AGU PUBLICATIONS

JGR

Journal of Geophysical Research: Space Physics

RESEARCH ARTICLE

10.1002/2015JA021027

Solar wind plasma interaction with Gerasimovich lunar magnetic anomaly

Shahab Fatemi[1,2], Charles Lue[3,4], Mats Holmström[3], Andrew R. Poppe[1,2], Martin Wieser[3], Stas Barabash[3], and Gregory T. Delory[1,2]

[1]Space Sciences Laboratory, University of California, Berkeley, California, USA, [2]Solar System Exploration Research Virtual Institute, NASA Ames Research Center, Moffett Field, California, USA, [3]Swedish Institute of Space Physics, Kiruna, Sweden, [4]Department of Physics, Umeå University, Umeå, Sweden

Key Points:
- The first local hybrid simulations of realistic lunar crustal magnetic fields
- Effects of low and high solar wind dynamic pressures on the Gerasimovich anomaly
- Electrostatic potential and solar wind flux distribution on the lunar surface

Correspondence to:
S. Fatemi,
shahab@ssl.berkeley.edu

Citation:
Fatemi, S., C. Lue, M. Holmström, A. R. Poppe, M. Wieser, S. Barabash, and G. T. Delory (2015), Solar wind plasma interaction with Gerasimovich lunar magnetic anomaly, *J. Geophys. Res. Space Physics*, *120*, doi:10.1002/2015JA021027.

Received 21 JAN 2015
Accepted 8 MAY 2015
Accepted article online 16 MAY 2015

Abstract We present the results of the first local hybrid simulations (particle ions and fluid electrons) for the solar wind plasma interaction with realistic lunar crustal fields. We use a three-dimensional hybrid model of plasma and an empirical model of the Gerasimovich magnetic anomaly based on Lunar Prospector observations. We examine the effects of low and high solar wind dynamic pressures on this interaction when the Gerasimovich magnetic anomaly is located at nearly 20° solar zenith angle. We find that for low solar wind dynamic pressure, the crustal fields mostly deflect the solar wind plasma, form a plasma void at very close distances to the Moon (below 20 km above the surface), and reflect nearly 5% of the solar wind in charged form. In contrast, during high solar wind dynamic pressure, the crustal fields are more compressed, the solar wind is less deflected, and the lunar surface is less shielded from impinging solar wind flux, but the solar wind ion reflection is more locally intensified (up to 25%) compared to low dynamic pressures. The difference is associated with an electrostatic potential that forms over the Gerasimovich magnetic anomaly as well as the effects of solar wind plasma on the crustal fields during low and high dynamic pressures. Finally, we show that an antimoonward Hall electric field is the dominant electric field for ~3 km altitude and higher, and an ambipolar electric field has a noticeable contribution to the electric field at close distances (<3 km) to the Moon.

1. Introduction

It is known that the Earth's Moon currently does not have a global intrinsic magnetic field, but it has localized remnant crustal magnetization [*Dyal et al.*, 1970; *Mihalov et al.*, 1971; *Hood et al.*, 2001]. Lunar crustal fields are extensively spread over the entire lunar surface with various field intensities, but they are mostly clustered on the southern hemisphere of the lunar far side [*Richmond and Hood*, 2008; *Mitchell et al.*, 2008; *Tsunakawa et al.*, 2010]. The maximum strength of these fields on the lunar surface is expected to be at least a few hundred nT [*Dyal et al.*, 1974; *Hood et al.*, 2001; *Mitchell et al.*, 2008].

The interaction between the solar wind plasma and lunar crustal fields is different from that of a planetary magnetosphere. The difference stems from the fact that the spatial scale of lunar crustal fields is smaller than the lunar radius and, on average, has an intermediate scale between the solar wind electron and ion gyro-radii. Therefore, the incident solar wind electrons are deflected and reflected by the crustal fields at higher altitudes compared to protons that penetrate deeper into the magnetic anomalies [*Siscoe and Goldstein*, 1973; *Saito et al.*, 2012; *Bamford et al.*, 2012]. This forms a charge separation and results in the formation of electrostatic fields over magnetized areas, which decelerate, deflect, and reflect ions above the crustal fields [*Halekas et al.*, 2011; *Lue et al.*, 2011; *Saito et al.*, 2012; *Futaana et al.*, 2013; *Deca et al.*, 2014].

Kaguya spacecraft observations at ~25 km altitude over the South Pole-Aitken basin crustal magnetic fields estimated an antimoonward electrostatic potential of ~+150 V above the Kaguya spacecraft altitude [*Saito et al.*, 2012]. They observed that the solar wind ions are decelerated over the crustal fields and reflected nonadiabatically with higher temperatures and lower bulk velocities than the incident solar wind ions. Kaguya and Chandrayaan-1 satellite observations indicated that, on average, about 10% of the incident solar wind proton flux is reflected in charged form over the crustal magnetic fields [*Saito et al.*, 2010; *Lue et al.*, 2011]. The ion reflection over the strongest fields can be 50% or more [*Lue et al.*, 2011], whereas <1% of the ions reflect in charged form from the unmagnetized lunar surface [*Saito et al.*, 2008; *Lue et al.*, 2014]. This implies that the

lunar surface can be shielded from the solar wind plasma under some of the strongest magnetic anomalies [*Lin et al.*, 1998; *Halekas et al.*, 2008; *Saito et al.*, 2010; *Wieser et al.*, 2010; *Vorburger et al.*, 2012].

Energetic neutral atom (ENA) imaging of the Moon from Chandrayaan-1 observations showed that a partial void of the solar wind plasma, a minimagnetosphere, forms above one of the strongest lunar magnetic anomalies located at the Crisium antipode near the Gerasimovich crater, known as Gerasimovich magnetic anomaly [*Wieser et al.*, 2010; *Vorburger et al.*, 2012; *Futaana et al.*, 2013]. They showed that the ENA flux was substantially reduced above the magnetic anomalies, while it was increased in the surrounding regions, indicating plasma deflection around crustal fields. By studying the energy spectrum of the ENA population, they estimated an electrostatic potential of larger than +135 V inside the Gerasimovich magnetic anomaly [*Futaana et al.*, 2013]. They also found that the Gerasimovich magnetic anomaly possesses a clearer correlation between the incident plasma parameters and the surface shielding efficiency compared to the other crustal fields, which is presumably due to its simple magnetic field topology compared to the other crustal fields, especially compared to the South Pole-Aitken basin region [*Vorburger et al.*, 2012]. This makes the Gerasimovich magnetic anomaly a favorable crustal field to study plasma interaction with lunar crustal magnetic fields [*Vorburger et al.*, 2012].

Apart from observations, several attempts have been made to model the solar wind plasma interaction with lunar magnetic anomalies theoretically, numerically, and experimentally using single dipole [*Siscoe and Goldstein*, 1973; *Harnett and Winglee*, 2000, 2002; *Poppe et al.*, 2012; *Kallio et al.*, 2012; *Wang et al.*, 2012, 2013; *Shaikhislamov et al.*, 2013; *Jarvinen et al.*, 2014; *Deca et al.*, 2014; *Ashida et al.*, 2014] and multidipole [*Harnett and Winglee*, 2003] approximations. Generally, these models, consistent with observations, have shown that strong magnetic anomalies may shield the lunar surface from solar wind and have a direct impact on surface weathering and swirl albedo markings [*Blewett et al.*, 2011; *Poppe et al.*, 2012]. Recently, *Jarvinen et al.* [2014] using a three-dimensional hybrid model studied the interaction between a single magnetic dipole mimicking the Gerasimovich magnetic anomaly. Their studies, consistent with Chandrayaan-1 ENA observations, estimated an electrostatic potential of <+300 V above the magnetic anomalies. They showed that an antimoonward Hall electric field ($\mathbf{J} \times \mathbf{B}/\rho$) forms this potential, which was also suggested by *Saito et al.* [2012] and *Shaikhislamov et al.* [2013] from MHD theory. Similarly, *Deca et al.* [2014] used a three-dimensional implicit electromagnetic particle-in-cell model to study the interaction between the solar wind and a spatially smaller magnetic dipole compared to Gerasimovich. They found the formation of a minimagnetosphere above the magnetic dipole and showed that about 10% of the incident solar wind ions are reflected by the magnetic fields, which is roughly consistent with observations [*Halekas et al.*, 2008; *Lue et al.*, 2011; *Saito et al.*, 2012]. They suggested that the minimagnetosphere is temporarily unstable to the mirror instabilities driven by pressure anisotropies [*Deca et al.*, 2014]. However, none of the models mentioned earlier have taken into account the actual crustal magnetic field strength and orientation.

Since lunar crustal magnetic fields are nondipolar and have complex field structures [*Hood et al.*, 2001; *Mitchell et al.*, 2008], studying the solar wind interaction with localized crustal fields requires more precise information about the topology of these fields. Both Lunar Prospector and Kaguya satellite observations at altitudes of 100 km and lower provided global maps of lunar magnetization, taken when the Moon was inside the Earth's magnetosphere and the crustal fields were not disturbed by solar wind plasma [*Hood et al.*, 2001; *Mitchell et al.*, 2008; *Tsunakawa et al.*, 2010]. Lunar Prospector observations were corrected and normalized to 30 km altitude [*Richmond and Hood*, 2008], while Kaguya observations were normalized to 100 km altitude [*Tsunakawa et al.*, 2010]. Later, empirical models based on the altitude-normalized observations were developed to construct models of the internal magnetic fields of the Moon [*Purucker*, 2008; *Purucker and Nicholas*, 2010; *Tsunakawa et al.*, 2014]. These models correlate well with observations and can be used to estimate the strength and orientation of the magnetic anomalies at any specific altitude, latitude, and longitude above the Moon.

Here we use a three-dimensional self-consistent hybrid plasma model [*Holmström*, 2010; *Holmström et al.*, 2012] and include the empirical model of lunar crustal magnetization developed by *Purucker and Nicholas* [2010] into our model to study the solar wind interaction with a localized lunar crustal field. Since the interaction with Gerasimovich magnetic anomaly has been more extensively studied compared to the other crustal fields [*Wieser et al.*, 2010; *Vorburger et al.*, 2012; *Futaana et al.*, 2013], and due to its relatively simple magnetic field structure, we focus on the solar wind interaction with the Gerasimovich magnetic anomaly. We examine the effects of low and high solar wind dynamic pressures on this interaction and study the surface shielding efficiency. We provide a map of the solar wind flux impacting on the lunar surface and we show how the elec-

trostatic charge distributes over the magnetized areas to deflect and reflect the solar wind. In the following sections, first, we explain our model and geometry of the Gerasimovich magnetic fields. Then we present our simulation results and discuss the physics of the interaction.

2. Model

We use a three-dimensional self-consistent hybrid plasma model, where the ions are kinetic macroparticles and electrons are a mass-less charge neutralizing fluid. In our model ion position, $\mathbf{r}_i$, and velocity, $\mathbf{v}_i$, are computed from the equation of motion (Lorentz force),

$$\frac{\mathrm{d}}{\mathrm{d}t}\begin{bmatrix}\mathbf{v}_i\\ \mathbf{r}_i\end{bmatrix}=\begin{bmatrix}\frac{q_i}{m_i}(\mathbf{E}+\mathbf{v}_i\times\mathbf{B})\\ \mathbf{v}_i\end{bmatrix}, \tag{1}$$

where m_i and q_i are respectively ion mass and charge, and $\mathbf{B}$ and $\mathbf{E}$ are the magnetic and electric fields. The electric field is given by,

$$\mathbf{E}=\frac{1}{\rho_i}\left(-\mathbf{J}_i\times\mathbf{B}+\mu_0^{-1}(\nabla\times\mathbf{B})\times\mathbf{B}-\nabla p_e\right)+\frac{\eta}{\mu_0}\nabla\times\mathbf{B}, \tag{2}$$

where ρ_i is the ion charge density, $\mathbf{J}_i$ is the ion current density, p_e is the electron pressure, and η is the resistivity. Finally, the magnetic field is obtained from Faraday's law. We assume that the plasma resistivity is zero and that there is a large resistivity inside the Moon. Then in the absence of plasma, i.e., inside the Moon and in the vacuum region in the lunar wake, Faraday's law becomes

$$\frac{\partial\mathbf{B}}{\partial t}=-\nabla\times\left(\frac{\eta}{\mu_0}\nabla\times\mathbf{B}\right), \tag{3}$$

which is a diffusion equation for the magnetic field. The stability condition for the diffusion equation requires $\Delta t < \mu_0\Delta x^2/2\eta$, where Δt [s] is the simulation time step, $\mu_0 = 4\pi\times10^{-7}$ (H/m) is the permeability of free space, Δx (m) is the simulation cell size, and η (Ω m] is the resistivity of the Moon (for more details about our model, see *Holmström* [2013] and *Fatemi et al.* [2014]).

To model the interaction with the Gerasimovich magnetic anomaly we assume that the lunar surface is a flat plane. Then we feed the Gerasimovich crustal fields map from the *Purucker and Nicholas* [2010] empirical model, which is a spherical harmonic model based on Lunar Prospector fluxgate magnetometer observations, into the three-dimensional configuration space of our hybrid model. This empirical lunar crustal magnetic field model, as explained in detail by *Purucker* [2008] and *Purucker and Nicholas* [2010], provides a spherical harmonic scalar magnetic potential to degree and order N, which is expressed as

$$V=R_L\sum_{n=1}^{N}\left(\frac{R_L}{r}\right)^{(n+1)}\sum_{m=0}^{n}(g_n^m\cos(m\phi)+h_n^m\sin(m\phi))P_n^m(\cos\theta), \tag{4}$$

where R_L = 1737.1 km is the mean radius of the Moon, r, ϕ, and θ are the radial distance to the center of the Moon, longitude, and colatitude in spherical coordinate system, respectively, and $P_n^m(\cos\theta)$ is the Schmidt quasi-normalized associated Legendre function of degree n and order m. The parameters g_n^m and h_n^m are the spherical harmonic coefficients estimated by *Purucker and Nicholas* [2010], and $N = 170$ produces a robust correlation between the model results and Lunar Prospector observations. *Purucker and Nicholas* [2010] introduced two different approaches in their calculations: a sequential method in which the original amplitudes of the magnetic field signals are best preserved, and a coestimate method that has better feature recognition compared to the sequential method but underestimates the signal amplitudes. Since the strength of the crustal fields is our primary interest, we use the sequential approach in our simulations. Finally, we calculate the crustal magnetic fields numerically from the gradient of the scalar magnetic potential expressed in equation (4). This approach ensures that $\nabla\cdot\mathbf{B}=0$. Figure 1 shows the Gerasimovich magnetic field magnitude from the *Purucker and Nicholas* [2010] model at three different altitudes and the coordinate system we use here. In this coordinate system, the $+x$ axis is normal to the surface of the Moon, the $+z$ axis points to the north polar axis, and the $+y$ axis points east in the equatorial plane and completes a right-handed coordinate system.

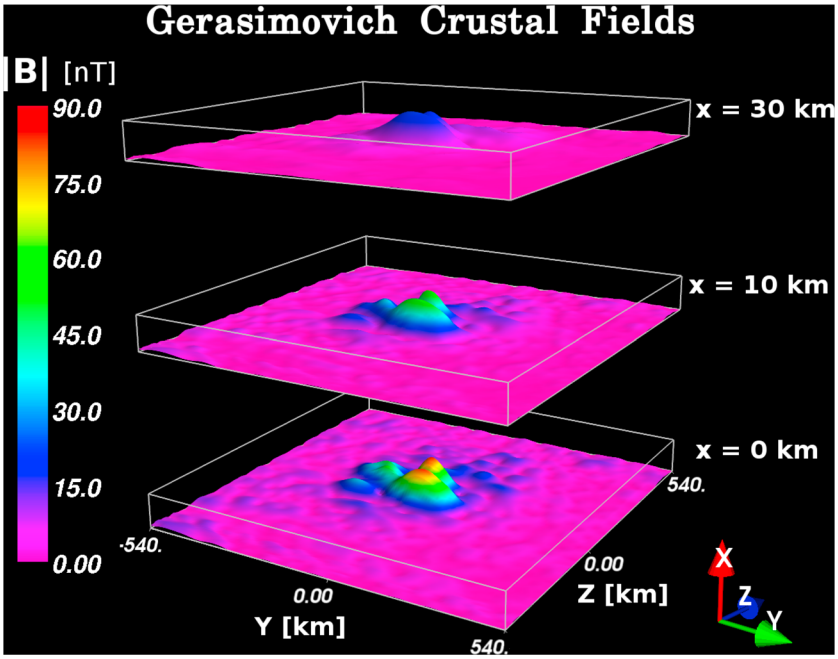

Figure 1. Undisturbed lunar crustal magnetic field magnitude at the Crisium antipode near the Gerasimovich crater, known as the Gerasimovich magnetic anomaly, obtained from *Purucker and Nicholas* [2010] model and applied into our hybrid model. Different plates show the crustal field strength at $x = 0$ km (at the surface) and 10 km and 30 km above the surface. The $+x$ axis is normal to the surface, $+z$ axis points the north polar axis, and $+y$ axis completes the right-hand coordinate system.

The center of the Gerasimovich magnetic anomaly, as well as the center of our coordinate system, is approximately located at 20.0°S, 123.5°W in the Selenographic (lunar geographical) coordinate system, and it covers an area of >200 km radius on the lunar surface [e.g., *Hood et al.*, 2001; *Blewett et al.*, 2011]. Due to Gerasimovich's geographical location, the solar wind flows with an inclination to the local surface normal vector ($+x$ axis). In our model, we assume that Gerasimovich is at 20° solar zenith angle (20° south of the subsolar point), and we take into account the solar wind aberration angle.

In this study, we employ a $320 \times 1080 \times 1080$ km^3 simulation domain (-50 km $< x < +270$ km, -540 km $< (y, z) < +540$ km), which is large enough compared to the spatial scale of Gerasimovich, as seen in Figure 1. We divide our simulation domain into a Cartesian grid with cubic cells of size 10 km ($\sim 0.2 r_g$, where $r_g = m_i v_{\mathrm{th}}/q_i B$ is the solar wind proton thermal gyroradius, and v_{th} and B are solar wind thermal velocity and undisturbed magnetic field magnitude, respectively). At the inflow boundary of the simulation box (yz plane at $x = +270$ km), kinetic macroparticles (protons) follow a Maxwellian velocity distribution function, and the upstream solar wind conditions remain constant during the simulation. We assume the Moon is a resistive object with resistivity $\eta = 10^7\ \Omega$ m [*Hood et al.*, 1982], and the lunar surface is a perfect plasma absorber. If a particle impacts the surface ($x = 0$), it is removed from the simulation domain. This is a reasonable approximation because we primarily study plasma interaction with a localized lunar crustal magnetic field, where <1% solar wind ion reflection from the lunar surface [*Saito et al.*, 2008; *Lue et al.*, 2014] can be neglected in comparison with ~10% average ion reflection from lunar crustal fields [*Lue et al.*, 2011]. However, *Holmström et al.* [2010] showed that the solar wind ion reflection from the lunar surface does not have any noticeable effect on the lunar plasma environment. We use 32 macroparticles per cell at the inflow boundary and advance their trajectories in small time steps ($\Delta t < 50$ μs).

However, 32 macroparticles per cell are not enough to provide high-resolution velocity distributions, yet increasing the number of particles per cell makes our simulations computationally very expensive (with the current configuration, every simulation run takes approximately 32,000 CPU hours). Therefore, after our hybrid simulations reached a quasi steady state solution ($t > 10$ s), we use a test particle model and inject

Table 1. Averaged Solar Wind Plasma Parameters During Chandrayaan-1 Observations on 17 June 2009 Applied in Our Model (See the Text)

Parameters	Symbols	Values	Units
Solar wind velocity vector	(u_x, u_y, u_z)	(−273.9, −44.3, −133.8)	km/s
Solar wind bulk speed	$\lvert\mathbf{u}_{sw}\rvert$	308.2	km/s
Solar wind B field vector	(B_x, B_y, B_z)	(−2.5, +2.9, 0.3)	nT
Solar wind B field magnitude	$\lvert\mathbf{B}_{sw}\rvert$	3.85	nT
Convective E field	(E_x, E_y, E_z)	(−0.37, −0.41, 0.90)	mV/m
Number density	n_{sw}	6.99	cm^{-3}
Proton temperature	T_p	2.4	eV
Electron temperature	T_e	9.8	eV
Proton thermal speed	v_{th}	21.4	km/s
Proton thermal gyroradius	r_g	57.9	km
Proton gyrofrequency	Ω_g	0.07	Hz
Dynamic pressure	P_{dyn}	1.11	nPa

256 macroparticles per cell with a Maxwellian velocity distribution at the inflow boundary of the simulation box (*yz* plane at $x = +270$ km), using exactly the same method as we have used in our hybrid model to load the particles in the simulation domain. We follow the trajectories of particles using the steady state electromagnetic fields obtained from our hybrid simulations for $t > 10$ s. This enables us to construct high-resolution velocity distributions and calculate the moments of the velocity distribution with appropriate statistics at any altitude of interest above the lunar surface.

2.1. Simulation Parameters

We used solar wind conditions during the Chandrayaan-1 observation over the Gerasimovich magnetic anomaly on 17 June 2009, which has been extensively studied before by *Wieser et al.* [2010], *Vorburger et al.* [2012], and *Futaana et al.* [2013]. These parameters are listed in Table 1 and were obtained from the Wind spacecraft measurements during the Chandrayaan-1 observation (between 17:30 UT and 22:50 UT), time shifted to the Moon and averaged over the observation period. The geographical location of Gerasimovich magnetic anomaly during this observation was at ∼20° solar zenith angle [*Wieser et al.*, 2010], which is consistent with our model assumptions.

In order to investigate the effects of low and high dynamic pressures on the solar wind interaction with Gerasimovich, we constructed three different simulations based on the parameters in Table 1. The first simulation run, termed the medium dynamic pressure run hereafter, has all the upstream solar wind parameters exactly the same as those listed in Table 1, where the solar wind dynamic pressure is 1.11 nPa. For the second and the third simulation runs we, respectively, decreased and increased the dynamic pressure to 0.63 nPa and 2.53 nPa by varying the plasma density only. We did not change the upstream solar wind speed for these simulations in order to keep the incident energy of the particles constant. A summary of these three simulation runs is listed in Table 2.

3. Results

Here we present our simulation results for the solar wind plasma interaction with the Gerasimovich magnetic anomaly for medium solar wind dynamic pressure condition (1.11 nPa) and compare our results with two cases when the solar wind dynamic pressure is lower (0.63 nPa) and higher (2.53 nPa) than the medium case.

Table 2. Upstream Solar Wind Dynamic Pressure Used in Three Simulation Runs

Simulation Run	Dynamic Pressure
Low	0.63 nPa
Medium	1.11 nPa
High	2.53 nPa

Figure 2 shows our simulation results for the medium dynamic pressure run at 3 km altitude above the surface. Figure 2a shows the undisturbed crustal magnetic fields magnitude ($|\mathbf{B}_m|$) over the Gerasimovich magnetic anomaly. These fields are obtained from the *Purucker and Nicholas* [2010] empirical model. Figure 2b shows the magnitude of

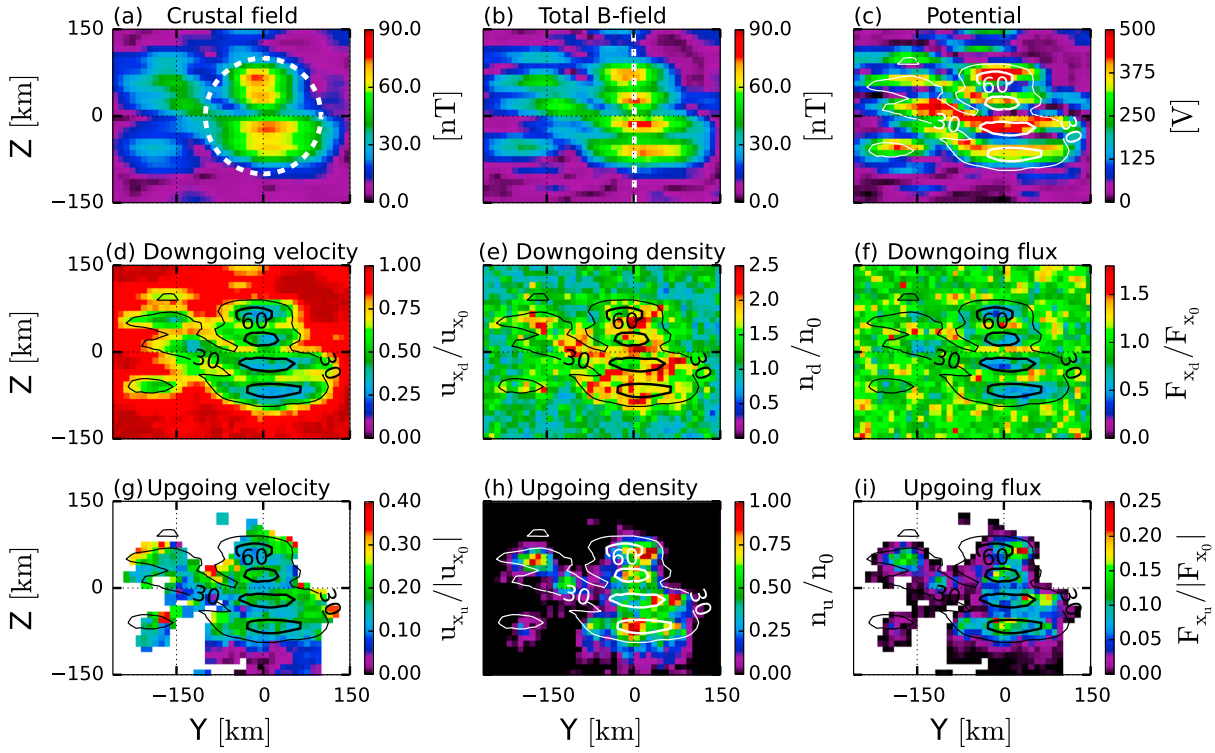

Figure 2. Hybrid simulation results during the medium dynamic pressure simulation in the *yz* plane at $x = 3$ km, viewed from the $+x$ direction. Simulation parameters are listed in Table 1, and the solar wind dynamic pressure for this run is 1.11 nPa. (a) Undisturbed Gerasimovich magnetic field strength $|\mathbf{B}_m|$; (b) total magnetic field magnitude $|\mathbf{B}_m + \mathbf{B}_{sw}|$; (c) electrostatic potential distribution from $-\int(\mathbf{E}_x - \mathbf{E}_{sw}) \cdot dx$; (d) normalized velocity of solar wind protons that are moving down toward the Moon (all particles with $u_x \leq 0$); (e) normalized density of the downgoing solar wind protons; (f) normalized flux of the downgoing solar wind protons, where $\mathbf{F}_{xd} = n_{xd}\mathbf{u}_{xd}$; (g) normalized velocity of solar wind protons that are moving up away from the Moon (all particles with $u_x > 0$); (h) normalized density of the upgoing solar wind protons; (f) normalized flux of the upgoing solar wind protons. The white dashed circle in Figure 2a shows the area within which we averaged the moments of distributions presented in Figures 6, 7, 9, and 10. The white straight dashed line in Figure 2b shows where we present our results in Figure 5. The contour lines plotted over Figures 2c–2i show the strength of the total magnetic fields. The outer contours (thin lines) show 30 nT, and the inner contours (thick lines) show 60 nT magnetic fields.

the total magnetic fields ($|\mathbf{B}_m + \mathbf{B}_{sw}|$), and Figure 2c shows the electrostatic potential distribution that forms at 3 km altitude with respect to our simulation inflow boundary ($x = +270$ km). By comparing Figure 2a with Figure 2b, we see that the crustal fields are compressed and disturbed by the solar wind. Figures 2d–2i show the moments of the velocity distribution at 3 km altitude, normalized to the upstream parameters listed in Table 1 for the solar wind protons moving down into the surface of the Moon (we only selected particles with $u_x \leq 0$), and moving up and going away from the Moon (only particles with $u_x > 0$), respectively. The contour lines plotted over Figures 2c–2i show the strength of the total magnetic fields. The outer contours show 30 nT, and the inner contours show 60 nT magnetic fields.

We see from Figures 2d and 2e that the downgoing protons are decelerated ~70% over the areas of the strong magnetic fields (≥60 nT, inside the inner contours), while the proton density is increased to ~2.5 times the solar wind density outside the strongest magnetic fields (outside the inner contours). This indicates that the plasma has been deflected around the strong magnetic field. Our simulations show that the lateral scale for plasma deflection around the Gerasimovich magnetic anomaly is at most 80 km for the medium solar wind dynamic pressure run. Moreover, we see from Figure 2f that the moonward solar wind flux is decreased more than 50% over the strongest fields (inside the inner contours), and we expect that less than this amount impacts the lunar surface due to additional proton deceleration and reflection below 3 km. This shows that the lunar surface is locally shielded >50% from incident solar wind flux within the strongest magnetic fields. Figures 2g–2i show that the solar wind protons are reflected over the crustal fields with lower velocities but higher densities compared to the undisturbed solar wind. These reflected protons are coming from 3 km and below, and as Figure 2i shows, their flux at some localized regions reaches nearly 20% of the incident solar wind flux.

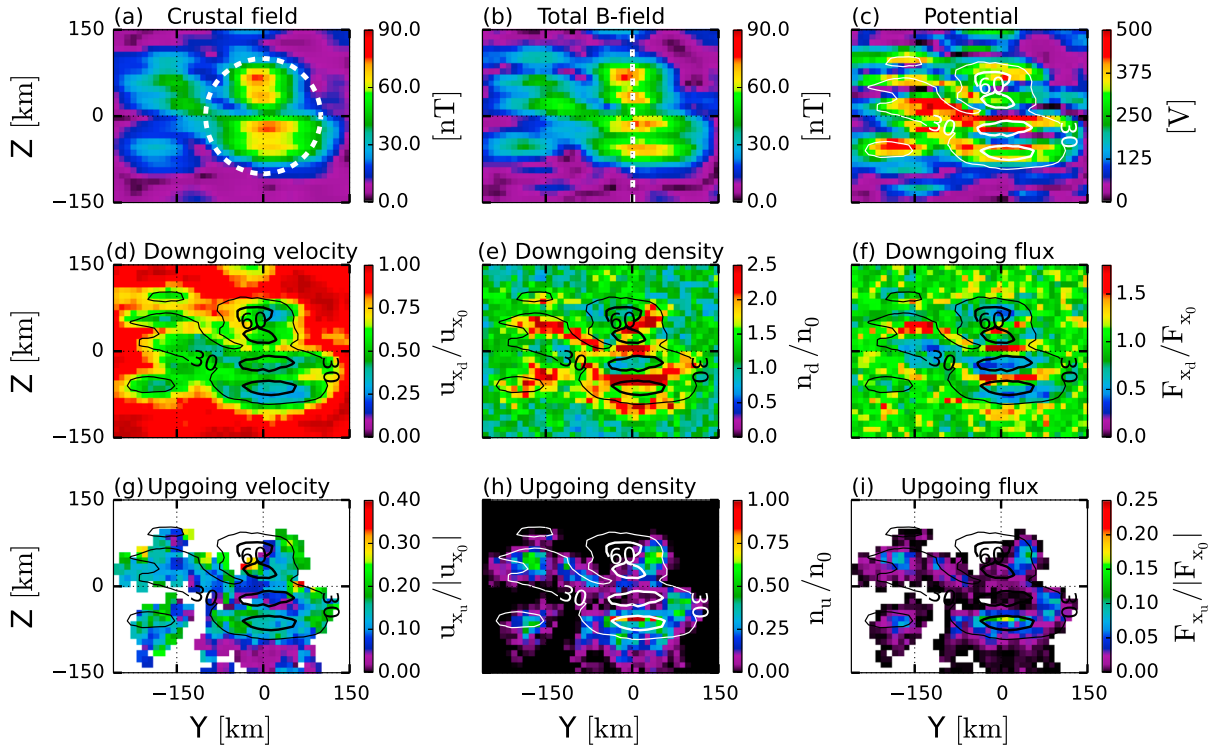

Figure 3. Hybrid simulation results during the low dynamic pressure case (0.63 nPa) in the *yz* plane at $x = 3$ km, viewed from the $+x$. The geometry of the cuts are the same as those in Figure 2.

Similar to Figure 2, Figures 3 and 4 show the details of our simulation results at 3 km altitude for the low and high dynamic pressures, respectively. We see from Figure 3b that the magnetic fields are less disturbed and compressed during the low dynamic pressure compared to the high dynamic pressures (Figures 2b and 4b). We also see from Figure 3e that the solar wind proton density is enhanced around the strong magnetic fields (outside the inner contours) for low dynamic pressure, while the density enhancement occurs over the strong magnetic fields (inside the inner contours) for high dynamic pressures, shown in Figure 4e. Figure 4i shows that the flux of reflected protons over some localized areas of the crustal fields exceeds 20% of the incident flux during high dynamic pressure, while Figure 3i does not show any significant proton reflection for low dynamic pressure. This is because the crustal fields and their associated electric fields are more compressed during high dynamic pressures and get stronger close to the surface compared to the low dynamic pressures. Strong electric fields close to the surface for high dynamic pressures reflect more particles compared to low dynamic pressures, as we can see by comparing Figure 4i with Figure 3i. In addition, since the magnetic fields are more compressed during high solar wind dynamic pressures, the reflection area over the crustal fields shrinks for the high dynamic pressures compared to the low dynamic pressures (compare the reflection area from Figure 3i with Figure 4i).

In order to distinguish the effects of low and high dynamic pressures, we compare the total magnetic field magnitude, downgoing plasma density, velocity, and flux for the three different dynamic pressure cases along the dashed line shown in Figure 2b and present our results in Figure 5. Generally, we see from Figure 5a that the undisturbed crustal fields (dashed line) are disturbed by the solar wind. However, the magnetic fields are less disturbed and compressed over the magnetic anomalies during the low dynamic pressure case compared to the high dynamic pressure case. Figure 5b shows that the solar wind protons are decelerated over the crustal fields, and we see an apparent anticorrelation between proton deceleration and magnetic field reduction over the crustal fields. As we explained earlier, we see that the solar wind protons are less decelerated over the crustal magnetic fields for the high dynamic pressure case compared to the low dynamic pressure case. Figure 5c shows that the solar wind proton density increases over the crustal fields. By comparing Figure 5c with Figure 5a, we see a correlation between density enhancement and magnetic field reduction over the crustal fields for the low dynamic pressure case, which suggests that the solar wind protons are more

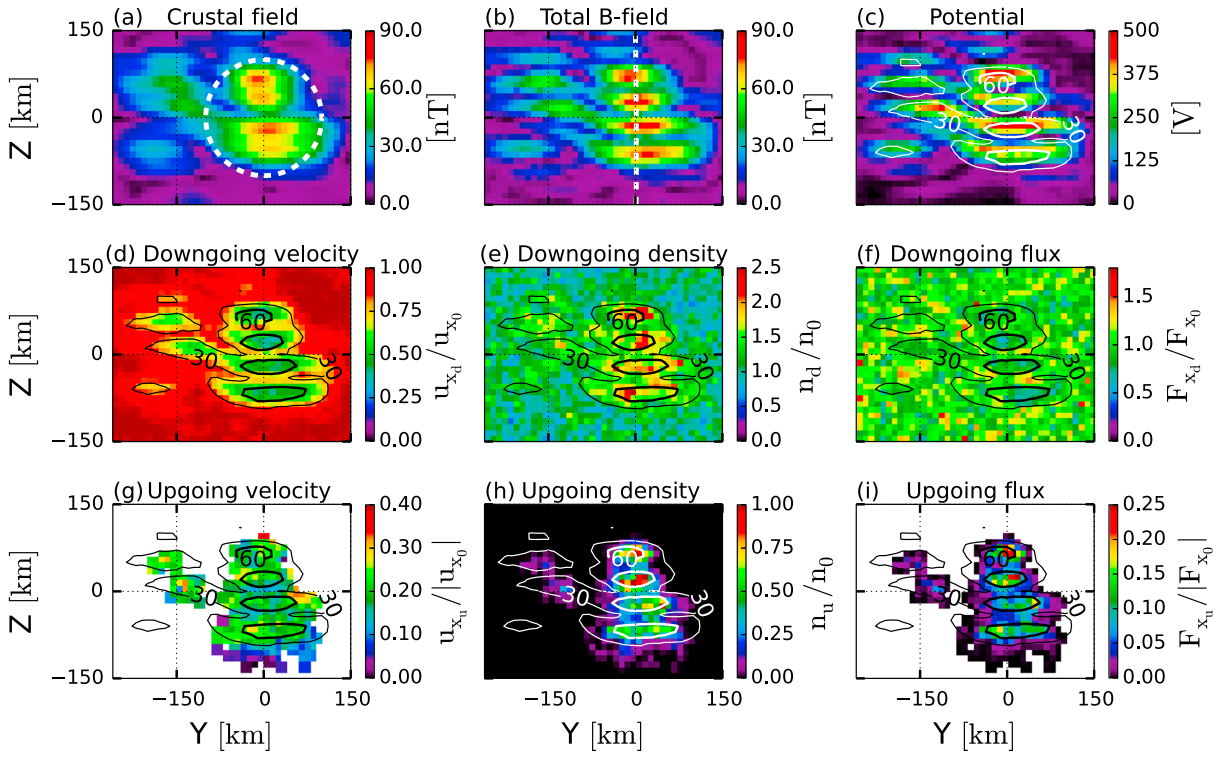

Figure 4. Hybrid simulation results during the high dynamic pressure case (2.53 nPa) in the *yz* plane at $x = 3$ km, viewed from the $+x$. The geometry of the cuts are the same as those in Figure 2.

deflected around the strongest crustal fields for the low dynamic pressure compared to those for the high dynamic pressure case. We see from Figure 5d that the moonward solar wind flux for the low dynamic pressure case is drastically reduced over the strong magnetized regions (> 60 nT), followed by a flux increase in the surrounding areas. The flux alternation over the crustal fields is clearly pronounced for the low dynamic pressure run, while there is not a significant amount of flux reduction over the crustal fields for the high dynamic pressure case.

Since the undisturbed Gerasimovich crustal fields extend from the surface to very high altitudes (theoretically to infinity), our modeled phenomena at low altitudes are connected to the physics of the interaction at higher and lower altitudes than that presented in Figures 2–5. Therefore, we calculated the moments of the velocity distribution as well as the field magnitudes from the surface to 200 km altitude. We averaged the moments over the white dashed circle of 100 km radius shown in Figures 2a, 3a, and 4a for every 1 km vertical distance. The results of this study are shown in Figures 6 and 7.

Figure 6a shows that the crustal magnetic fields are compressed and disturbed by the solar wind as a function of distance from the surface. Obviously, the fields get stronger close to the surface when the dynamic pressure is increased, but one would expect the fields to be weaker at high altitudes during high dynamic pressure compared to low dynamic pressure, which is not the case here. We previously showed that the reflected flux during high dynamic pressures is higher compared to low dynamic pressures. Analogous to particle reflection from comets and planetary objects, reflected protons from lunar crustal fields interact with the incoming solar wind plasma, forming instabilities that result in increased magnetic fields at high altitudes during high dynamic pressures [e.g., *Hoppe and Russell*, 1982; *Gary et al.*, 1988; *Halekas et al.*, 2006; *Fatemi et al.*, 2014].

Figure 6b compares the vertical component of the electric field ($\mathbf{E}_x$) built up by the solar wind interaction with the crustal fields for the three different solar wind dynamic pressures. We see that the electric field during the low dynamic pressure case is higher than that for high dynamic pressures at high altitudes (>20 km) above the surface. Therefore, the solar wind ions start to decelerate at higher altitudes during low dynamic pressures compared to high dynamic pressures. The decelerated particles are then deflected by the crustal fields, and thus, we see that the particles are more deflected around the strong crustal fields during low dynamic

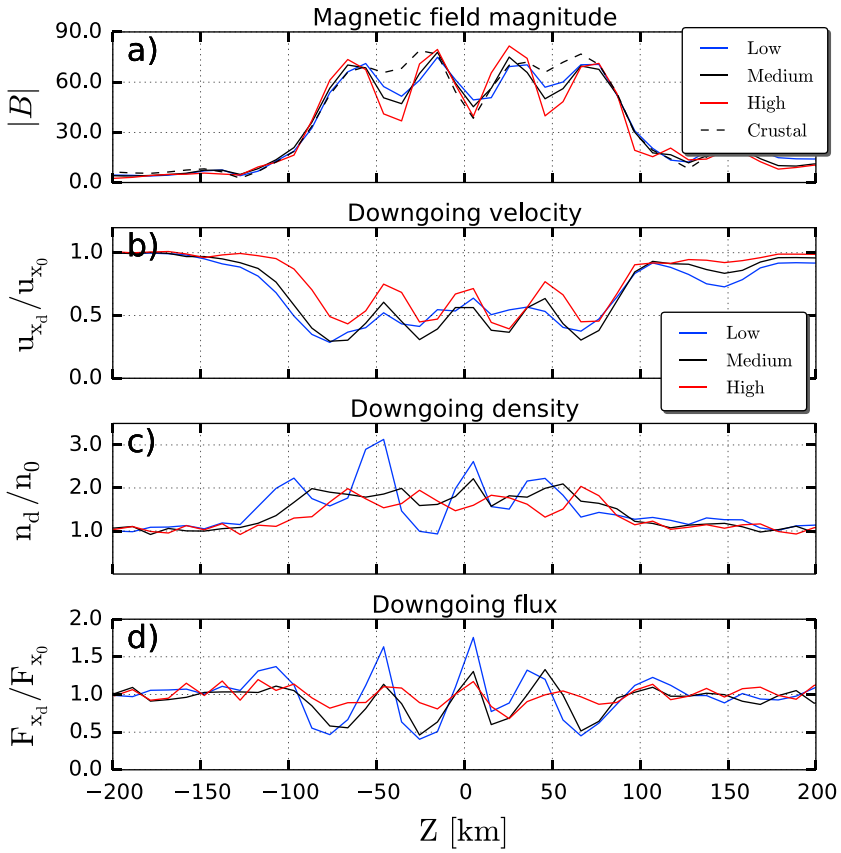

Figure 5. The magnetic field and calculated moments of the velocity distribution along the white dashed line shown in Figure 2b. The quantities are taken at $(x, y) = (3, 0)$ km along the z axis. (a) Magnitude of the magnetic fields, (b) normalized downgoing solar wind proton velocity, (c) normalized downgoing solar wind proton density, and (d) normalized downgoing solar wind proton, for the low (blue), medium (black), and high (red) solar wind dynamic pressure simulations. The dashed line in Figure 5a shows the magnitude of the undisturbed crustal magnetic fields.

pressures compared to high dynamic pressures, as seen by comparing Figure 3e with Figure 4e. However, the electric field closer to the surface (<10 km) is stronger for high dynamic pressures compared to low dynamic pressures. Therefore, the ions are reflected more during high dynamic pressures compared to low dynamic pressures, as we see by comparing Figure 3i with Figure 4i.

We calculated the electrostatic potential by integrating the electric fields presented in Figure 6b, and the results are shown in Figure 6c. We see that, on average, a potential of nearly +300 V forms at the surface under the Gerasimovich crustal fields; however, this potential changes as the solar wind dynamic pressure varies. Since we averaged the electric fields over a fixed area for every 1 km altitude, and since the magnetic fields are compressed more during high dynamic pressures and cover smaller areas compared to low dynamic pressures, the averaged electrostatic potential at the surface during the high dynamic pressure case seems smaller than that for the low dynamic pressure case. However, our simulations suggest (not shown here) a maximum electrostatic potential of over +585 V forms at localized areas at the surface during the high dynamic pressure, whereas a maximum of about +510 V forms locally during the low dynamic pressure (see Table 3 for maximum local field strength at the surface during different solar wind dynamic pressures).

In Figure 7, we compare the averaged downgoing moments (Figures 7a and 7c) and averaged upgoing moments (Figures 7d and 7f) between the low, medium, and high dynamic pressure runs. Figure 7a shows that the downgoing proton density starts increasing at nearly 40 km altitude for the low dynamic pressure run, and it remains larger than the proton density of the other runs down to nearly 4 km altitude, which is consistent with the electric field pattern shown in Figure 6b. As soon as the fields get stronger for the higher dynamic pressure runs, the density increases more and overtakes that of the low dynamic pressure run. Similarly, we see from Figure 7b that the particles are decelerated as they pass over the crustal fields and their

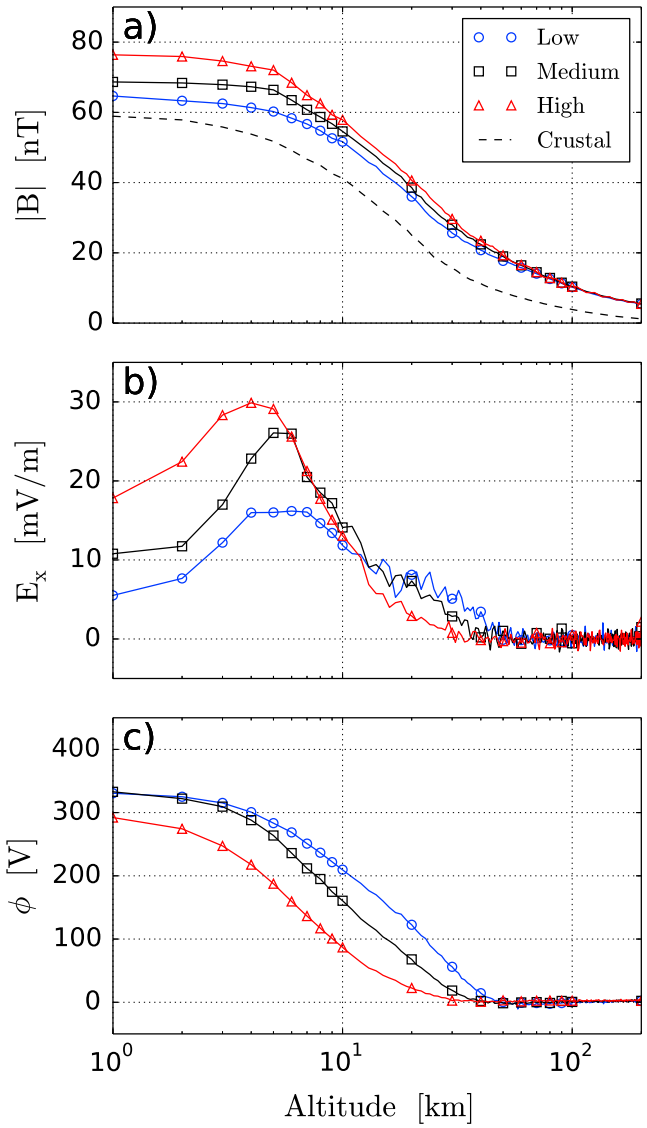

Figure 6. (a) Averaged magnetic field magnitude, (b) veraged vertical component of the electric field $\mathbf{E}_x$, and (c) averaged electrostatic potential over the white dashed circle shown in Figure 2a from 1 km to 200 km altitude above the lunar surface for the low (blue), medium (black), and high (red) dynamic pressure simulations. Dashed line in Figure 6a is the averaged undisturbed crustal fields over the Gerasimovich magnetic anomaly. The electrostatic potential distribution is calculated from $\phi = -\int (\mathbf{E}_x - \mathbf{E}_{sw}) \cdot dx$.

velocity reduces to nearly 50% of the incident solar wind velocity. We see that the particle deceleration at high altitudes (>20 km) during the low dynamic pressure run is higher than that during the high dynamic pressure run. Figure 7c shows that the averaged incident flux of particles impacting the lunar surface below the crustal fields is reduced by nearly 10% during low dynamic pressure and ~5% during high dynamic pressure. This shows that the lunar surface within Gerasimovich magnetic anomaly is, on average, shielded ≤10% from the solar wind flux.

Figure 7d shows that the altitude of the maximum solar wind proton reflection over the Gerasimovich magnetic anomaly reduces from 4 km above the surface for low dynamic pressure to nearly 2 km during high dynamic pressure. Since the magnetic fields are stronger for the medium dynamic pressure run at low altitudes (below 10 km) compared to the low dynamic pressure run, the density of the reflected protons is larger than that of the low dynamic pressure run. However, when we increased the dynamic pressure for the high dynamic pressure run, the fields are more compressed into the surface, and the solar wind protons are affected by the crustal fields at lower altitudes compared to the low dynamic pressure run. Therefore, the density of

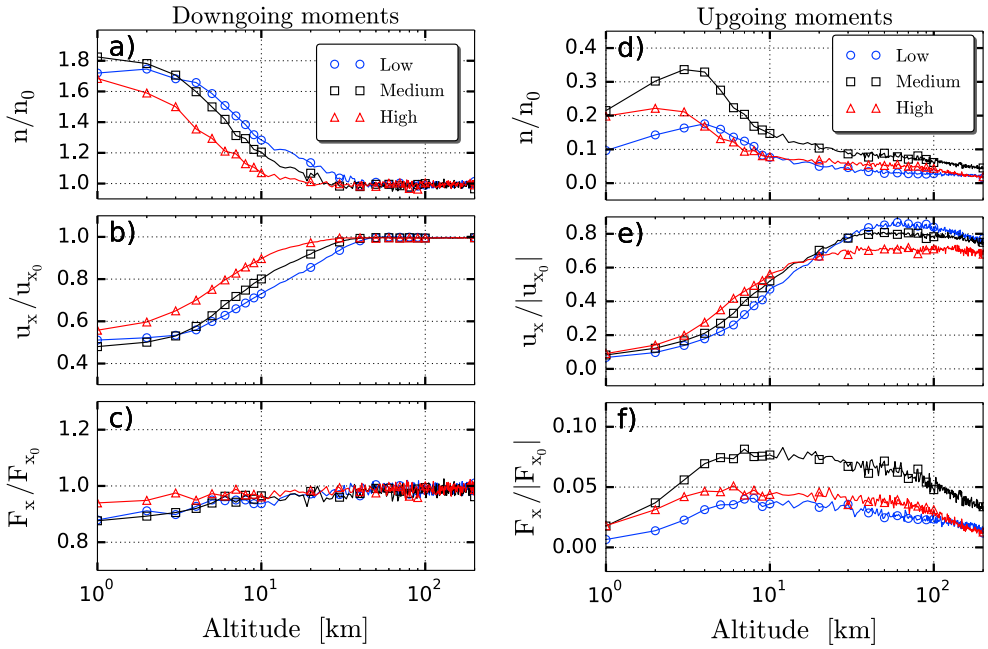

Figure 7. Averaged moments of the velocity distribution over the white dashed circle shown in Figure 2a from 1 km to 200 km altitude above the lunar surface for the low (blue), medium (black), and high (red) dynamic pressure simulations. (a–c) Downgoing and (d–f) upgoing moments. Normalized proton density (Figures 7b and 7d), normalized proton velocity (Figures 7a and 7e), and normalized proton flux (Figures 7c and 7f).

the reflected protons for the high dynamic pressure run is not as high as the medium dynamic pressure run. On the other hand, since the fields are stronger for the high dynamic pressure run, Figure 7e shows that the reflected protons are more accelerated over the crustal fields compared to the low dynamic pressure case. Figure 7f shows that, on average, less than 10% of the solar wind flux is reflected over the Gerasimovich anomaly. Since most of the reflected protons at high altitudes (>30 km) move out from our averaging area (the white dashed circle in Figure 2a) and are picked up by the solar wind, we cannot accurately calculate their moments. Therefore, we see large reductions of reflected proton density, velocity, and flux in our simulation results in Figures 7d–7f at high altitudes (>50 km). Figure 8 shows how the reflected protons over Gerasimovich magnetic anomaly move away from the Moon and are picked up by the solar wind. Some of these particles come back down and impact the surface, but we have not seen any of them become subject to a second reflection within the anomaly region.

In order to investigate more details about the solar wind interaction with the Gerasimovich magnetic anomaly, Figure 9 shows the energy spectra of the solar wind protons at four different altitudes integrated over the white area shown in Figure 2a for the medium pressure simulation run. Figure 9a shows the energy distribution of downgoing protons only. We see that protons are decelerated and heated as they move into the crustal fields. Low-energy solar wind ions are decelerated over the crustal fields, and their kinetic energy is converted to magnetic and thermal energy. High-energy ions, though, pass through the crustal fields and impact the lunar surface. Our moment calculations show that the heating process approximately starts from 40 km altitude (not shown here), where the electrostatic fields start decelerating protons as seen in Figure 6b. The average proton temperature of the solar wind protons at 3 km altitude is nearly 29 eV, which is 12 times higher than the incident solar wind proton temperature. Figure 9b shows the energy distribution of reflected protons. We see that the reflected protons have a higher temperature and lower bulk velocity than the incident solar wind protons, which is consistent with Kaguya observations [*Saito et al.*, 2012]. However, our model

Table 3. Maximum Values at the Lunar Surface Under the Gerasimovich Magnetic Anomaly

	Low	Medium	High
Total magnetic field (B_m+B_{sw}) (nT)	82.24	85.95	91.87
Electrostatic potential (V)	512.31	556.05	586.71
Upward electric field (mV/m)	36.07	39.75	45.08
Surface shielding efficiency	84%	75%	59%

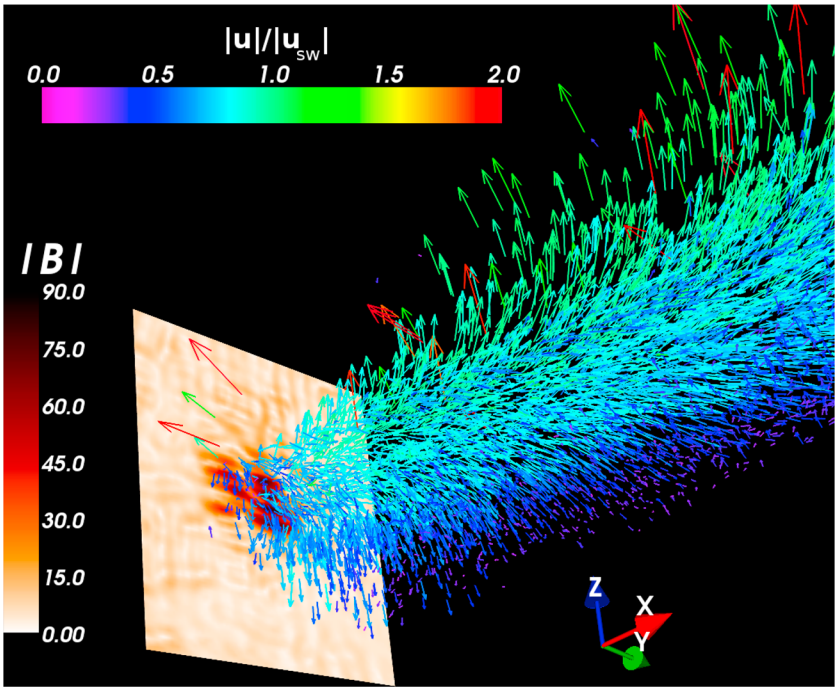

Figure 8. A snapshot of the reflected protons' direction of motion for the medium dynamic pressure run. The flat plane shows the magnitude of the magnetic fields at the lunar surface, and vectors show the direction of motion of the reflected protons above the Gerasimovich magnetic anomaly in our entire simulation domain. Vector length and their colors indicate the normalized velocity of the reflected protons $|\mathbf{u}|/|\mathbf{u}_{sw}|$.

shows that the average proton temperature for reflected protons at Kaguya's observation altitude (25 km) is about two times larger than the solar wind temperature, while Kaguya observed reflected protons with a temperature nearly 4 times larger than the incident solar wind temperature [*Saito et al.*, 2012]. This is probably because the solar wind temperature was nearly 5 times higher during the Kaguya observation compared to the condition used in our model. In addition, the Kaguya observation was made over the South Pole-Aitken basin region, which has different magnetic field strength and topology compared to the Gerasimovich magnetic anomaly.

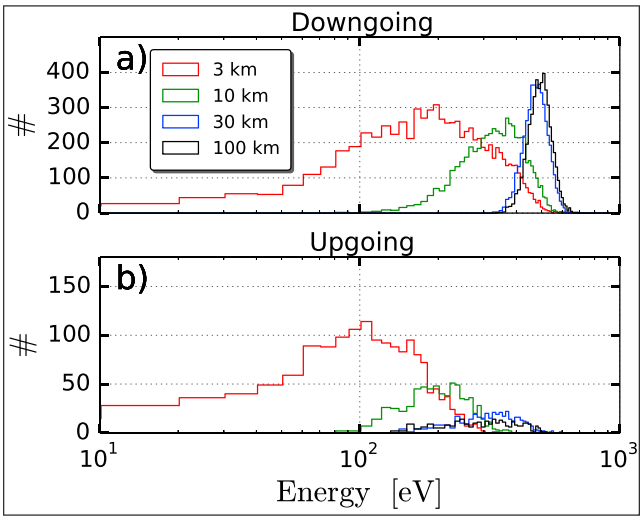

Figure 9. Energy spectra of solar wind protons at 3 km (red), 10 km (green), 30 km (blue), and 100 km (black) altitudes above the lunar surface. (a) Only the downgoing (moonward) protons, and (b) only the upgoing (antimoonward) protons are selected over the white circle shown in Figure 2a.

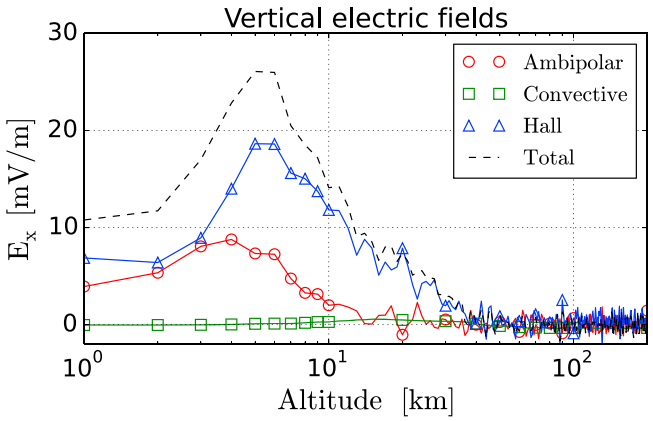

Figure 10. Vertical profile of the electric field terms from equation (2) for the medium dynamic pressure simulation. Ambipolar $\nabla p_e/\rho_i$ (red), convective $\mathbf{J}_i \times \mathbf{B}/\rho_i$ (green), hall $\mathbf{J} \times \mathbf{B}/\rho_i$ (blue) electric fields. The dashed line is the sum of the three electric field terms. The Ohmic term ($\eta \nabla \times \mathbf{B}/\mu_0$) shown in equation (2) is zero above the lunar surface because plasma resistivity $\eta = 0$ and, thus, not shown here.

Previous theoretical calculations [*Saito et al.*, 2012; *Shaikhislamov et al.*, 2013] and hybrid simulations [*Jarvinen et al.*, 2014] suggested that the Hall term is the dominant electric field over the lunar crustal fields. In our model the electric field (equation (2)) contains four different electric terms: the Hall ($\mathbf{J} \times \mathbf{B}/\rho_i$), ambipolar ($\nabla p_e/\rho_i$), convective ($\mathbf{J}_i \times \mathbf{B}/\rho_i$), and Ohmic ($\eta \nabla \times \mathbf{B}/\mu_0$) electric fields. Figure 10 compares the vertical component (along the *x* axis) of these terms as a function of height for the medium dynamic pressure simulation run. Since the solar wind resistivity is zero, the Ohmic term is zero, and hence, not shown here. Our model shows that the Hall term is the dominant electric field but only for ~3 km altitude and higher. We see that the ambipolar electric field, which is not included in the *Jarvinen et al.* [2014] model, has a noticeable contribution to the electric field at close distances to the Moon, and consequently on the total vertical electric field and its associated ion deceleration and plasma reflection over the crustal fields. However, all of these terms reach their maximum at some distance above the surface, suggesting the formation of an electrostatic layer over crustal fields above the surface, which we have also seen from Figure 6b. This electrostatic layer forms above the surface mainly due to the nondipolar topology of the Gerasimovich anomaly, which reveals the importance of including realistic magnetic anomaly topology in this study.

4. Discussion

We studied for the first time the solar wind plasma interaction with localized lunar crustal fields using an empirical model of lunar crustal magnetization applied in our hybrid model. We focused on the interaction with the Gerasimovich magnetic anomaly because its interaction with the solar wind has been observed before [*Wieser et al.*, 2010; *Vorburger et al.*, 2012; *Futaana et al.*, 2013]. In addition, Gerasimovich has a relatively simple magnetic field structure compared to other crustal fields, especially the South Pole-Aitken basin, yet it is one of the strongest ones known today. Moreover, since the closest strong crustal fields to Gerasimovich anomaly are nearly 800 km away (e.g., see the lunar crustal magnetization map in *Mitchell et al.* [2008, Figure 4]), there are no external field disturbances on the Gerasimovich anomaly from nearby crustal fields other than the solar wind.

The main difference between the presented results in this study and all the other numerical simulations presented in the past is the realistic crustal fields we have used in our simulations. We have shown that the undisturbed crustal magnetic fields are significantly modified by the solar wind. By comparing Figures 2b, 3b, and 4b, we also showed that the field compression is higher during high dynamic pressures (see Table 3 for maximum field strength at the surface during different solar wind dynamic pressures). These changes indicate the importance of using electromagnetic plasma solvers to understand the physics of this interaction and also implies that test particle simulations are not appropriate for modeling of such interactions.

Collisionless shock theories of solar wind plasmas predict a measure of the thickness of the interaction region $L_0 = A\delta_e$, where δ_e is the electron inertial length, and A is empirically estimated to be $A \lesssim 5$ [*Barnes et al.*, 1971]. For the solar wind conditions we applied in our model (Table 1), $\delta_e \simeq 2$ km and $L_0 \lesssim 10$ km, thus the choice

of our simulation cell size (10 km) is approximately right. If a crustal field has a sufficiently large characteristic length scale $L_m \gg L_0$, the solar wind interacts with it, compresses it, and possibly forms a local shock [*Tidman*, 1967]. The characteristic length for Gerasimovich, as seen in Figure 2a, is $L_m \geq 200$ km, which makes it a suitable example to study the solar wind plasma interaction with a lunar crustal field using hybrid models.

Since the size of the Gerasimovich magnetic anomaly is smaller than the ion gyroradius and larger than the electron gyroradius, electrons reach a high $\mathbf{E} \times \mathbf{B}$ drift velocity and carry most of the electric current. While the solar wind ions penetrate deep into the crustal fields, electrons are deflected and/or reflected at higher altitudes compared to ions because of their lighter mass, resulting in a charge separation and formation of electric fields normal and tangential to the lunar surface [*Siscoe and Goldstein*, 1973; *Saito et al.*, 2012; *Deca et al.*, 2014]. In addition, the lunar surface is expected to be charged differently compared to unmagnetized regions because of this charge separation, and the resulting electric field can modify the near-surface physics of the interaction. Since the electrons are a charge-neutralizing fluid in our hybrid model, we cannot investigate the influence of surface charging on the plasma interaction with magnetic anomalies. However, the results presented in this study, as well as those presented by *Fatemi et al.* [2012] in the lunar wake, show that our hybrid model is able to observe ambipolar electric fields forming due to charge separation.

In order to stop the solar wind flow at or above the surface, $B_m^2/2\mu_0 > m_i n_{sw} u_{sw}^2$, where B_m is the crustal magnetic field magnitude, m_i is the solar wind ion mass, and n_{sw} and u_{sw} are solar wind number density and bulk speed, respectively. For the solar wind conditions listed in Table 1, B_m needs to be larger than 53 nT to stagnate the solar wind flow. As we can see from Figure 2a, the typical length scales of the crustal fields that are stronger than 53 nT are not large enough to stagnate the solar wind and form a strong local shock. Figure 6a also shows that the average magnitude of the undisturbed Gerasimovich magnetic fields (dashed line) drops below 50 nT at 5 km above the surface. We do not see any signature of shock formation above Gerasimovich, which is generally consistent with observations [*Ness et al.*, 1968; *Colburn et al.*, 1971]. However, observations and simulations have suggested that some of the crustal fields might be strong enough to form a minimagnetosphere [*Lin et al.*, 1998; *Harnett and Winglee*, 2002, 2003; *Kurata et al.*, 2005; *Halekas et al.*, 2008; *Bamford et al.*, 2012], and some under special solar wind plasma conditions and lunar orientation form collisionless shocks [*Lin et al.*, 1998; *Fatemi et al.*, 2014; *Halekas et al.*, 2014]. Our simulations suggest that if any local shock forms over Gerasimovich, it would be either at the surface or at very close distances to the Moon.

Minimum electrostatic potentials (ϕ_s) required to theoretically stop the solar wind flow over a crustal field can be obtained from the ion equation of motion:

$$-e\phi_s = \frac{1}{2} m_i v_{sw}^2. \tag{5}$$

By applying equation (5) into the pressure balance equation for compressible plasmas, we get

$$\phi_s = -\frac{B_m^2}{4e\mu_0 n_{sw}}, \tag{6}$$

where the negative sign indicates that the direction of ϕ_s is opposite to the solar wind flow direction. Assuming B_m = 53 nT and n_{sw} = 6.99 cm^{-3} (from Table 1), then $|\phi_s| \simeq 500$ V, which is larger than the average electrostatic potential we calculated from our simulation results in Figure 6b. While we have found potentials larger than 500 V at localized areas over Gerasimovich (see Table 3), the spatial scale of those areas is not large enough and, thus, they cannot completely stop the solar wind but, rather, largely contribute to plasma deflection and reflection over the crustal fields. Chandrayaan-1 ENA observations estimated a global electrostatic potential of nearly 250 V at the surface of the Gerasimovich magnetic anomaly [*Futaana et al.*, 2013], which is roughly consistent with our simulation results.

We showed in Figures 2–4 that the electrostatic potential over the crustal fields deflects the solar wind particles around the crustal fields and, if strong enough, reflects them upstream. If the fluxes of the reflected charged particles are large enough, they interact with the upstream solar wind and generate electromagnetic waves and plasma instabilities [e.g., see *Halekas et al.*, 2006; *Tsugawa et al.*, 2012]. These waves interact with both the solar wind and the reflected particles, compress the magnetic fields and plasma upstream, and deflect the solar wind flow around magnetized areas [*Halekas et al.*, 2013; *Fatemi et al.*, 2014; *Halekas et al.*, 2014]. Our simulations, however, show that the magnetic field and plasma enhancement over the crustal fields

is partly due to the crustal field compression and solar wind deceleration and partly due to the interaction of protons reflected from crustal fields. A more detailed analysis of the wave activities and plasma instabilities forming in particle models above crustal fields is required to investigate the role of plasma reflection over crustal fields, which is outside the scope of this study.

We showed in Figure 7f that the flux of reflected particles is increased as the dynamic pressure increases. This is because the crustal fields are more compressed during high dynamic pressures. Table 3 shows the strongest fields at the surface, as well as the maximum surface shielding efficiency from the solar wind flux, and compares them for the three different dynamic pressures we examined in our model. We see that for the high dynamic pressures, the electric and magnetic fields at the surface are stronger and the impacting flux to the surface is larger compared to the low dynamic pressures. This explains the large densities and velocities of the reflected particles during high dynamic pressure in Figures 2 and 4 compared to low dynamic pressure in Figure 3. However, since the fields are compressed and their effective area is reduced during the high dynamic pressures and since our averaging area (the white circle in Figure 2a) is fixed, our moment calculations in Figure 7 show lower reflection flux during the high dynamic pressure run compared to the medium pressure run. This statement holds for all panels in Figure 7. Nevertheless, if the solar wind dynamic pressure is very high, such that it confines all the crustal fields into the lunar surface, the whole solar wind flux will impact the lunar surface without being distorted and/or reflected.

Figures 2–5 presented our simulation results on a plane at 3 km altitude above the lunar surface, which is approximately the height where most of the plasma reflection takes place (see Figure 7d), electric field reaches a maximum (Figure 6b), and the ambipolar electric field becomes comparable to the hall electric field (Figure 10). We also explained the effects of solar wind dynamic pressure on the fields and plasma at that certain place. However, the presented results will change as we move toward or away from the Moon, which is due to the physics of the interaction. Since showing the simulation results at any altitude above the lunar surface within the format of those presented in Figures 2-5 is not doable, we presented a profile of our results as a function of height above the lunar surface in Figures 6, 7, 9, and 10 from averaging over a constant area shown by the white dashed circle of radius 100 km in Figures 2a, 3a, and 4a. The quantitative values of the presented results in those figures will change if the averaging area is highly modified. We chose this area such that it covers all the undisturbed crustal fields with magnetic field strength $B_m \geq 53$ nT at the surface (the minimum required fields to stop the solar wind flow), and we chose it as a circle to have a simple geometry. We examined the effects of choosing circles with 75 km, 125 km, and 150 km radii, as well as squares with 75 km, 125 km, and 150 km sides, and we did not observe significant differences in the general conclusions we drew from our presented results here. However, if the radius of the averaging area becomes larger than the spatial scale of the Gerasimovich magnetic anomaly (>200 km), or small enough such that it does not cover most of the strong crustal fields, the quantitative values of the results presented in Figures 6, 7, 9, and 10, and their associated conclusions will be significantly altered.

Our simulations showed that for low dynamic pressures there is a large flux reduction over the strong crustal fields with a large flux enhancement (~40% of the incident solar wind) at the surrounding areas. Our model showed that the lateral scale of flux deflection around the crustal fields is at most 80 km (Figure 3f). In comparison, Chandrayaan-1 observations using ENA imaging showed that the Gerasimovich magnetic anomaly is surrounded by a large ENA enhancement nearly 300 km from the magnetized region [*Wieser et al.*, 2010; *Futaana et al.*, 2013]. This ENA enhancement is plausibly due to a large plasma deflection over the crustal fields [*Wieser et al.*, 2010]. Our simulations also suggested that the averaged surface-shielding efficiency below the crustal fields is around 10%, which is smaller than the estimated surface efficiency from Chandrayaan-1 ENA observations (~30% from *Vorburger et al.* [2012]). These differences between our simulations and observations are probably because the strength of the crustal fields at close distances to the surface are much stronger than the fields predicted by the *Purucker and Nicholas* [2010] empirical model, which we used in this study. No observations have been made below ~18 km over the Gerasimovich magnetic fields yet. Lunar Prospector remote measurements of the lunar surface fields using electron reflectometry technique [*Halekas et al.*, 2010], however, predict that the magnetic field strength on the lunar surface below the crustal fields, including Gerasimovich, may be a few hundred nT [*Mitchell et al.*, 2008; *Halekas et al.*, 2010]. This shows the importance of having future lunar missions fly over the lunar crustal fields at very low altitudes and the need for any landers or rovers to accurately measure the surface magnetic fields.

This study, consistent with observations [*Wieser et al.*, 2010; *Vorburger et al.*, 2012; *Futaana et al.*, 2013], suggests that lunar crustal fields locally shield the surface from impinging solar wind and form an electrostatic potential above the lunar surface. We examined the distribution of the solar wind flux impacting the lunar surface over the Gerasimovich magnetic anomaly and explained how the electrostatic fields are distributed. We examined the effects of varying dynamic pressure and showed that during high dynamic pressure the surface is overall less shielded from solar wind flux, yet more particles get reflected from the small regions of highest crustal field strength, unless the solar wind dynamic pressure is so high that it compresses all the crustal fields into the lunar surface. However, these results depend on the solar wind incidence angle and the direction of the solar wind magnetic field. Studying the effects of solar wind plasma incidence angle and the orientation of the solar wind magnetic field are left for future studies.

Acknowledgments

S. Fatemi, A. R. Poppe, and G. T. Delory gratefully acknowledge support from NASA's Solar System Exploration Research Virtual Institute (SSERVI), grant NNX14AG16A. This publication is SSERVI contribution SSERVI-2015-026. This research was conducted using resources provided by the Swedish National Infrastructure for Computing (SNIC) at the High Performance Computing Center North (HPC2N), Umeå University, Sweden. The software used in this work was developed in part by the DOE NNSA ASC- and DOE Office of Science ASCR-supported Flash Center for Computational Science at the University of Chicago. The visualization tools we developed for our model data analysis are based on python Matplotlib and Mayavi open libraries. The authors thank the International Space Science Institute (ISSI) Bern, Switzerland, for organizing a meeting when the topic of this paper was extensively discussed. We thank the teams who created and provided Wind magnetic field and plasma data used in this analysis, including K. W. Ogilvie, A. J. Lazarus, and R. Lepping. The Wind data used for this paper is available at Comprehensive Solar Wind Laboratory For Long-Term Solar Wind Measurements at NASA website wind.nasa.gov. Data set name: WIND SWE 92-sec and MFI Magnetic Field. Selection period is 17 June 2009 between 16:30 UT and 21:50 UT.

Yuming Wang thanks Mihaly Horanyi and another reviewer for their assistance in evaluating the paper.

References

Ashida, Y., H. Usui, I. Shinohara, M. Nakamura, I. Funaki, Y. Miyake, and H. Yamakawa (2014), Full kinetic simulations of plasma flow interactions with meso- and microscale magnetic dipoles, *Phys. Plasmas*, *21*, 122903.

Bamford, R., B. Kellett, W. Bradford, C. Norberg, A. Thornton, K. Gibson, I. Crawford, L. Silva, L. Gargaté, and R. Bingham (2012), Minimagnetospheres above the lunar surface and the formation of lunar swirls, *Phys. Rev. Lett.*, *109*(8), 081101.

Barnes, A., P. Cassen, J. D. Mihalov, and A. Eviatar (1971), Permanent lunar surface magnetism and its deflection of the solar wind, *Science*, *172*(3984), 716–718.

Blewett, D. T., E. I. Coman, B. R. Hawke, J. J. Gillis-Davis, M. E. Purucker, and C. G. Hughes (2011), Lunar swirls: Examining crustal magnetic anomalies and space weathering trends, *J. Geophys. Res.*, *116*, E02002, doi:10.1029/2010JE003656.

Colburn, D. S., J. D. Mihalov, and C. P. Sonett (1971), Magnetic observations of the lunar cavity, *J. Geophys. Res.*, *76*(13), 2940–2957.

Deca, J., A. Divin, G. Lapenta, and B. Lembége (2014), Electromagnetic particle-in-cell simulations of the solar wind interaction with lunar magnetic anomalies, *Phys. Rev. Lett*, *112*, 151102.

Dyal, P., C. W. Parkin, and C. P. Sonett (1970), Apollo 12 magnetometer: Measurement of a steady magnetic field on the surface of the moon, *Science*, *169*, 762–764.

Dyal, P., C. W. Parkin, and W. D. Daily (1974), Magnetism and the interior of the moon, *Rev. Geophys.*, *12*(4), 568–591.

Fatemi, S., M. Holmström, and Y. Futaana (2012), The effects of lunar surface plasma absorption and solar wind temperature anisotropies on the solar wind proton velocity space distributions in the low-altitude lunar plasma wake, *J. Geophys. Res.*, *117*, A10105, doi:10.1029/2011JA017353.

Fatemi, S., M. Holmström, Y. Futaana, C. Lue, M. R. Collier, S. Barabash, and G. Stenberg (2014), Effects of protons reflected by lunar crustal magnetic fields on the global lunar plasma environment, *J. Geophys. Res. Space Physics*, *119*, 6095–6105, doi:10.1002/2014JA019900.

Futaana, Y., S. Barabash, M. Wieser, C. Lue, P. Wurz, A. Vorburger, A. Bhardwaj, and K. Asamura (2013), Remote energetic neutral atom imaging of electric potential over a lunar magnetic anomaly, *Geophys. Res. Lett.*, *40*, 262–266, doi:10.1002/grl.50135.

Gary, S. P., C. D. Madland, N. Omidi, and D. Winske (1988), Computer simulations of two-pickup-ion instabilities in a cometary environment, *J. Geophy. Res.*, *93*(A9), 9584–9596.

Halekas, J. S., D. A. Brain, D. L. Mitchell, and R. P. Lin (2006), Whistler waves observed near lunar crustal magnetic sources, *Geophys. Res. Lett.*, *33*, L22104, doi:10.1029/2006GL027684.

Halekas, J. S., G. Delory, D. Brain, R. P. Lin, and D. L. Mitchell (2008), Density cavity observed over a strong lunar crustal magnetic anomaly in the solar wind: A mini-magnetosphere?, *Planet. Space Sci.*, *56*(7), 941–946.

Halekas, J. S., R. J. Lillis, R. P. Lin, M. Manga, M. E. Purucker, and R. A. Carley (2010), How strong are lunar crustal magnetic fields at the surface?: Considerations from a reexamination of the electron reflectometry technique, *J. Geophys. Res.*, *115*, E03006, doi:10.1029/2009JE003516.

Halekas, J. S., Y. Saito, G. T. Delory, and W. M. Farrell (2011), New views of the lunar plasma environment, *Planet. Space Sci.*, *59*(14), 1681–1694.

Halekas, J. S., A. R. Poppe, J. P. McFadden, and K. H. Glassmeier (2013), The effects of reflected protons on the plasma environment of the moon for parallel interplanetary magnetic fields, *Geophys. Res. Lett.*, *40*, 4544–4548, doi:10.1002/grl.50892.

Halekas, J. S., A. R. Poppe, J. P. McFadden, V. Angelopoulos, K.-H. Glassmeier, and D. A. Brain (2014), Evidence for small-scale collisionless shocks at the Moon from ARTEMIS, *Geophys. Res. Lett.*, *41*, 7436–7443, doi:10.1002/2014GL061973.

Harnett, E. M., and R. M. Winglee (2000), Two-dimensional MHD simulation of the solar wind interaction with magnetic field anomalies on the surface of the Moon, *J. Geophys. Res.*, *105*(A11), 24997–25007.

Harnett, E. M., and R. M. Winglee (2002), 2.5D Particle and MHD simulations of mini-magnetospheres at the Moon, *J. Geophys. Res.*, *107*(A12), 1421, doi:10.1029/2002JA009241.

Harnett, E. M., and R. M. Winglee (2003), 2.5-D fluid simulations of the solar wind interacting with multiple dipoles on the surface of the Moon, *J. Geophys. Res.*, *108*(A2), 1088, doi:10.1029/2002JA009617.

Holmström, M. (2010), Hybrid modeling of plasmas, in *Proceedings of ENUMATH 2009, the 8th European Conference on Numerical Mathematics and Advanced Applications, Uppsala, July 2009*, edited by G. Kreiss et al., pp. 451–458, Springer, Berlin.

Holmström, M. (2013), Handling vacuum regions in a hybrid plasma solver. ASTRONUM-2012, *ASP Conf. Ser.*, *474*, 202–207.

Holmström, M., M. Wieser, S. Barabash, Y. Futaana, and A. Bhardwaj (2010), Dynamics of solar wind protons reflected by the Moon, *J. Geophys. Res.*, *115*, A06206, doi:10.1029/2009JA014843.

Holmström, M., S. Fatemi, Y. Futaana, and H. Nilsson (2012), The interaction between the Moon and the solar wind, *Earth Planets Space*, *64*(2), 237–245.

Hood, L. L., F. Herbert, and C. P. Sonett (1982), The deep lunar electrical conductivity profile: Structural and thermal inferences, *J. Geophys. Res.*, *87*(B7), 5311–5326.

Hood, L. L., A. Zakharian, J. Halekas, D. L. Mitchell, R. P. Lin, M. H. Acuña, and A. B. Binder (2001), Initial mapping and interpretation of lunar crustal magnetic anomalies using Lunar Prospector magnetometer data, *J. Geophys. Res.*, *106*(E11), 27,825–27,839.

Hoppe, M. M., and C. T. Russell (1982), Planetary bow shock comparisons: Inferences from upstream waves, *Nature*, *295*(41), 5852.

Jarvinen, R., M. Alho, E. Kallio, P. Wurz, S. Barabash, and Y. Futaana (2014), On vertical electric fields at lunar magnetic anomalies, *Geophys. Res. Lett.*, *41*, 2243–2249, doi:10.1002/2014GL059788.

Kallio, E., et al. (2012), Kinetic simulations of finite gyroradius effects in the lunar plasma environment on global, meso, and microscales, *Planet. Space Sci.*, *74*(1), 146–155.

Kurata, M., H. Tsunakawa, Y. Saito, H. Shibuya, M. Matsushima, and H. Shimizu (2005), Mini-magnetosphere over the Reiner Gamma magnetic anomaly region on the Moon, *Geophys. Res. Lett.*, *32*, L24205, doi:10.1029/2005GL024097.

Lin, R. P., D. L. Mitchell, D. W. Curtis, K. A. Anderson, C. W. Carlson, J. McFadden, M. H. Acuña, L. L. Hood, and A. Binder (1998), Lunar surface magnetic fields and their interaction with the solar wind: Results from lunar prospector, *Science*, *281*(5382), 1480–1484.

Lue, C., Y. Futaana, S. Barabash, M. Wieser, M. Holmstrom, A. Bhardwaj, M. B. Dhanya, and P. Wurz (2011), Strong influence of lunar crustal fields on the solar wind flow, *Geophys. Res. Lett.*, *38*, L03202, doi:10.1029/2010GL046215.

Lue, C., Y. Futaana, S. Barabash, M. Wieser, A. Bhardwaj, and P. Wurz (2014), Chandrayaan-1 observations of backscattered solar wind protons from the lunar regolith: Dependence on the solar wind speed, *J. Geophys. Res. Planets*, *119*, 968–975, doi:10.1002/2013JE004582.

Mihalov, J. D., C. P. Sonett, J. H. Binsack, and M. D. Moutsoulas (1971), Possible fossil lunar magnetism inferred from satellite data, *Science*, *171*(3974), 892–895.

Mitchell, D. L., J. S. Halekas, R. P. Lin, S. Frey, L. L. Hood, M. H. Acuna, and A. Binder (2008), Global mapping of lunar crustal magnetic fields by Lunar Prospector, *Icarus*, *194*(2), 401–409.

Ness, N. F., K. W. Behannon, H. E. Taylor, and Y. C. Whang (1968), Perturbations of the interplanetary magnetic field by the lunar wake, *J. Geophys. Res.*, *73*(11), 3421–3440.

Poppe, A. R., J. S. Halekas, G. T. Delory, and W. M. Farrell (2012), Particle-in-cell simulations of the solar wind interaction with lunar crustal magnetic anomalies: Magnetic cusp regions, *J. Geophys. Res.*, *117*, A09105, doi:10.1029/2012JA017844.

Purucker, M. (2008), A global model of the internal magnetic field of the Moon based on Lunar Prospector magnetometer observations, *Icarus*, *197*(1), 19–23.

Purucker, M. E., and J. B. Nicholas (2010), Global spherical harmonic models of the internal magnetic field of the Moon based on sequential and coestimation approaches, *J. Geophys. Res.*, *115*, E12007, doi:10.1029/2010JE003650.

Richmond, N. C., and L. L. Hood (2008), A preliminary global map of the vector lunar crustal magnetic field based on Lunar Prospector magnetometer data, *J. Geophys. Res.*, *113*, E02010, doi:10.1029/2007JE002933.

Saito, Y., et al. (2008), Solar wind proton reflection at the lunar surface: Low energy ion measurement by MAP-PACE onboard SELENE (KAGUYA), *Geophys. Res. Let.*, *35*, L24205, doi:10.1029/2008GL036077.

Saito, Y., et al. (2010), In-flight performance and initial results of plasma energy angle and composition experiment (PACE) on SELENE (Kaguya), *Space Sci. Rev.*, *154*(1–4), 265–303.

Saito, Y., M. N. Nishino, M. Fujimoto, T. Yamamoto, S. Yokota, H. Tsunakawa, H. Shibuya, M. Matsushima, H. Shimizu, and F. Takahashi (2012), Simultaneous observation of the electron acceleration and ion deceleration over lunar magnetic anomalies, *Earth Planets Space*, *64*(2), 83–92.

Shaikhislamov, I. F., V. M. Antonov, Yu. P. Zakharov, E. L. Boyarintsev, A. V. Melekhov, V. G. Posukh, and A. G. Ponomarenko (2013), Mini-magnetosphere: Laboratory experiment, physical model and Hall MHD simulation, *Adv. Space Res.*, *52*(3), 422–436.

Siscoe, G. L., and B. Goldstein (1973), Solar wind interaction with lunar magnetic fields, *J. Geophys. Res.*, *78*(28), 6741–6748.

Tidman, D. A. (1967), Turbulent shock waves in plasmas, *Phys. Fluids*, *10*(3), 547.

Tsugawa, Y., et al. (2012), Statistical study of broadband whistler-mode waves detected by Kaguya near the Moon, *Geophys. Res. Lett.*, *39*, L16101, doi:10.1029/2012GL052818.

Tsunakawa, H., H. Shibuya, F. Takahashi, H. Shimizu, M. Matsushima, A. Matsuoka, S. Nakazawa, H. Otake, and Y. Iijima (2010), Lunar magnetic field observation and initial global mapping of lunar magnetic anomalies by MAP-LMAG onboard SELENE (Kaguya), *Space Sci. Rev.*, *154*(1–4), 219–251.

Tsunakawa, H., F. Takahashi, H. Shimizu, H. Shibuya, and M. Matsushima (2014), Regional mapping of the lunar magnetic anomalies at the surface: Method and its application to strong and weak magnetic anomaly regions, *Icarus*, *228*, 35–53.

Vorburger, A., P. Wurz, S. Barabash, M. Wieser, Y. Futaana, M. Holmström, A. Bhardwaj, and K. Asamura (2012), Energetic neutral atom observations of magnetic anomalies on the lunar surface, *J. Geophys. Res.*, *117*, A07208, doi:10.1029/2012JA017553.

Wang, X., M. Horányi, and S. Robertson (2012), Characteristics of a plasma sheath in a magnetic dipole field: Implications to the solar wind interaction with the lunar magnetic anomalies, *J. Geophys. Res.*, *117*, A06226, doi:10.1029/2012JA017635.

Wang, X., C. T. Howes, M. Horányi, and S. Robertson (2013), Electric potentials in magnetic dipole fields normal and oblique to a surface in plasma: Understanding the solar wind interaction with lunar magnetic anomalies, *Geophys. Res. Lett.*, *40*, 1686–1690, doi:10.1002/grl.50367.

Wieser, M., S. Barabash, Y. Futaana, M. Holmström, A. Bhardwaj, R. Sridharan, M. B. Dhanya, A. Schaufelberger, P. Wurz, and K. Asamura (2010), First observation of a mini-magnetosphere above a lunar magnetic anomaly using energetic neutral atoms, *Geophys. Res. Lett.*, *37*, L05103, doi:10.1029/2009GL041721.